



Tuning the CO₂ hydrogenation path by moderately phosphating the Co-Al catalyst toward methanol synthesis

Heng Zhang, Donglei Mao, Jinxin Zhang, Dongfang Wu^{*}

Department of Chemical Engineering, School of Chemistry and Chemical Engineering, Southeast University, Jiangning District, Nanjing 211189, China

ARTICLE INFO

Keywords:

Phosphating
Co-based catalyst
Methanol synthesis
CO₂ hydrogenation
Density functional theory

ABSTRACT

Regulating diversified reaction paths is one of the key challenges for commercial CO₂ hydrogenation. Herein, a phosphating strategy is proposed to modify the surface structure of a layered double hydroxide-derived Co-Al catalyst for CO₂ hydrogenation to CH₃OH. It is shown that moderate phosphating can achieve a uniform incorporation of P without damaging the original layered morphology and crystal structure. Experiments and density functional theory calculations demonstrate that a significant electron transfer occurs in the surface oxygen vacancies after phosphating, which promotes the direct hydrogenation of key intermediate H₃CO* to CH₃OH by constraining the cleavage of the C-O bond in H₃CO*. The CH₃OH selectivity and space-time yield are, therefore, substantially boosted after moderate phosphating, far superior to those on conventional Cu-, In₂O₃- and noble metal-based catalysts. This work provides valuable insights into the manipulation of reaction paths through the design and rational modification of catalytic materials.

1. Introduction

The emission of CO₂ has increased rapidly, due to the increase of world population and the rapid development of the technology industry in recent decades, which has caused a series of economic and environmental problems, especially the greenhouse effect [1]. Many efforts have been made to reduce the concentration of CO₂ and utilize it rationally, such as the capture and storage of CO₂ and hydrogenation of CO₂, among which selective CO₂ hydrogenation to methanol is considered as one of the effective and valuable ways to realize the recycling of carbon resources [2]. Methanol, as a substantial chemical green energy, can be not only utilized as a solvent in organic synthesis, but also as a basic primary material in the production of many important chemicals and excellent energy, such as formaldehyde, dimethyl carbonate (DMC), olefin, and methyl tert-butyl ether (MTBE) [3,4]. Moreover, as described in the “methanol economy” by Nobel Laureate George Olah [5], methanol synthesis by direct hydrogenation of CO₂ is a significant and promising strategy for the utilization of CO₂.

Since the commercial application of CuZnAl catalysts to methanol synthesis from syngas, Cu-based catalysts have been intensively and extensively investigated for the hydrogenation of CO₂ to methanol [6,7]. Indeed, Cu-based catalysts can drive the production of methanol in direct CO₂ hydrogenation, but some problems need to be solved,

especially the low selectivity of methanol caused by the competition of the reverse water gas reaction and the limited lifetime of the catalysts caused by the fast agglomeration and deactivation of the active metal Cu [8–12]. To enhance the catalytic performance, multi-metallic composite systems were constructed, such as CuO/ZnO/ZrO₂ [9], CuO/CeO₂/ZrO₂ [10], and Cu/ZnO/Al₂O₃/ZrO₂ [11], which serve to stabilize the active site of the catalysts and modulate the interfacial structure and surface properties of Cu-based catalysts. Actually, in addition to Cu-based catalysts, at the current stage, catalysts for the hydrogenation of CO₂ to methanol that have been also extensively investigated include supported noble-metal [13,14], In₂O₃-based [15–17], and intermetallic compound [18–20] catalysts. However, due to the expensive price of noble-metal catalysts [13,14] and the relatively low catalytic stability of In₂O₃-based catalysts [15], their large-scale application prospects are confined. In addition to further optimizing these catalysts to improve the reaction efficiency, the exploration of new catalytic materials is also a promising strategy to efficiently catalyze CO₂ hydrogenation to methanol. Especially, cobalt, a cheap and earth-abundant metal, and the potential of its application to hydrogenation of CO₂ to methanol have been largely overlooked.

Although cobalt is frequently utilized in CO₂ hydrogenation reactions because of its excellent CO₂ adsorption and C-O bond activation cleavage ability, the reaction product is typically methane or CO rather

^{*} Corresponding author.

E-mail address: dfwu@seu.edu.cn (D. Wu).

<https://doi.org/10.1016/j.apcatb.2023.123257>

Received 5 July 2023; Received in revised form 12 August 2023; Accepted 1 September 2023

Available online 4 September 2023

0926-3373/© 2023 Elsevier B.V. All rights reserved.

than methanol [21–24]. In recent years, it has been discovered that the potential of Co-based catalysts in the synthesis of methanol is of considerably exploratory value. Yang et al. [21], for instance, achieved the change of the main product by controlling the exposure of the Co_3O_4 crystal plane, and the selectivity of methanol reached up to ca. 30% at the optimal condition of 6 bar and 250 °C. However, the methanol synthesis performance of pure Co_3O_4 is poor, so further optimization is required to enhance more CO_2 selective hydrogenation toward methanol. A promising strategy to improve the catalytic performance of CO_2 hydrogenation to methanol is by the design and modification of active surface sites [25,26], such as incorporating other atoms to alter the charge distribution and electronic structure of the catalyst surface [22, 27]. For example, Li et al. [25] documented the existence of an active interface in the hybrid oxide catalyst of manganese and cobalt, which enhances the CO_2 hydrogenation to methanol at low pressure. Particularly, the addition of non-metals to modify the cobalt catalysts has also been shown to have sufficient potential to improve the performance of CO_2 hydrogenation [26,27]. As reported by Wang et al. [26], the cobalt species were modified via Co-O-SiO_n linkages with silica as a support and ligand, exhibiting a methanol selectivity of 70.5% at a CO_2 conversion of 8.6% under 320 °C and 2 MPa. In order to further unlock the potential of Co-based catalysts, it is worth more exploration to design a Co-based catalyst with an excellent structure for efficient catalytic CO_2 hydrogenation to methanol.

Furthermore, for cobalt oxide, the transition of the crystalline phase could occur at the appropriate reduction atmosphere (generally greater than 200 °C), resulting in a change in the active sites as well as the catalytic properties [21,28]. Thereby, it is crucial to preserve the catalyst stability, especially in the presence of reducing gas in the CO_2 hydrogenation reaction system. As is well known, aluminum, as the most common structural promoter, can prevent catalyst sintering by enhancing the stability of the crystals [28,29]. A Co-Al catalyst, especially prepared from layered double hydroxide (LDH) precursor, has not only an excellent structural stability but also the advantages of a large specific surface area [20], suitable alkalinity [23], and uniform elemental distribution [12], and thus it is a good candidate for CO_2 hydrogenation to methanol. Nevertheless, for the typical Co-Al catalyst, experiments and DFT calculations revealed that the CO_2 adsorbed on the oxygen vacancies could convert to the reaction intermediates such as formate and methoxy species, which are very susceptible to deep hydrogenation to CH_4 rather than the formation of CH_3OH [21,23]. To tune the hydrogenation path of CO_2 , modifying the surface structure of the catalyst by introducing P atoms is a plausible approach, especially since P atoms can be introduced at low temperatures and the amount of addition can be controlled during the phosphating treatment [30,31]. Moreover, P atoms can interact with metal to create transition metal phosphides (TMPs) with metalloid characteristics and excellent performance [31–33], and thus the catalyst would inevitably produce the charge movement and structural change after phosphating modification, which could effectively affect the H_2 activation, CO_2 adsorption as well as the structure change of the intermediates in the subsequent CO_2 hydrogenation process. With the above considerations in mind, the modification of the catalyst surface by non-metal P is rarely applied in the thermal catalysis of CO_2 hydrogenation, which is worthy of further investigation.

In the present work, the LDH-derived Co-Al catalysts were prepared, and the surfaces of these catalysts were modified with the controllable phosphating degree. The effects of the phosphating treatment on the crystal structures and properties of the catalysts were investigated by experiments and DFT calculations, and the hydrogenation paths over the catalysts before and after the surface modification were revealed. The results demonstrate that the uniform introduction of P by phosphating can cause electron migration on the surface of the catalysts, which can significantly alter the hydrogenation path of the key intermediate CH_3O^* , and accordingly greatly boost the catalytic performance in methanol synthesis.

2. Experimental section

2.1. Catalyst preparation

All the used chemicals were of analytical-reagent (AR) grade without further purification and were bought from Sinopharm Chemical Reagent Co., Ltd. (China). CuZnAl catalyst was prepared by a co-precipitation method, available in Text S1.

Fig. 1a depicts schematically the catalyst preparation process. The CoAlLDH precursor was synthesized by a urea hydrolysis method. Typically, 0.02 mol $\text{Co}(\text{NO}_3)_2 \cdot 6\text{H}_2\text{O}$, 0.01 mol $\text{Al}(\text{NO}_3)_3 \cdot 9\text{H}_2\text{O}$, and 0.04 mol NH_4F dissolved in 70 mL distilled water. 0.10 mol urea was then added to the aqueous solution under vigorous stirring. The as-prepared mixed solution was sealed in autoclaves and treated at 110 °C for 24 h. Afterward, the sediment was centrifuged, washed completely with distilled water, and dried at 80 °C for 12 h to get the LDH precursor. Finally, the powders, marked as CoAlLDH, were obtained after calcination at 450 °C for 3 h in a muffle furnace.

CoAlLDH-P_x samples were prepared by phosphating the obtained CoAlLDH directly. 200 mg CoAlLDH and a specified amount of NaH_2PO_2 were put into separate quartz boats, which were then placed in a tube furnace with the CoAlLDH on the downstream side of the tube furnace, as shown in Fig. S1. The catalysts with different phosphorus contents were obtained by varying the mass of sodium hypophosphite. The phosphating products obtained using 100, 150, 200, and 250 mg NaH_2PO_2 were denoted as CoAlLDH-P₁, CoAlLDH-P₂, CoAlLDH-P₃, and CoAlLDH-P₄, respectively. The phosphating experiments were carried out in N_2 flow at 350 °C using a temperature ramping rate of 2 °C min⁻¹, kept at this temperature for 2 h, and then cooled to room temperature.

2.2. Catalyst reduction and catalytic test

Catalyst reduction and catalytic tests were conducted in a stainless steel tubular fixed-bed reactor with an internal diameter of 0.8 cm. And the temperature of the fixed-bed reactor was controlled by a programmable thermal controller. 0.1 g of CoAlLDH or CoAlLDH-P_x catalyst (20–40 mesh), diluted with 0.4 g of SiC powder (20–40 mesh), was loaded into the fixed-bed reactor. The catalyst was heated to 300 °C at the rate of 10 °C min⁻¹ in 30 mL min⁻¹ H_2 flow and held at this temperature for 2 h. The reduced catalyst was named as CoAlLDH-R or CoAlLDH-P_x-R.

Following reduction, the reactor was cooled to room temperature, and CO_2 - H_2 - N_2 mixed gases (1:3:1, molar ratio) were inputted. The total pressure was raised to 3.0 MPa, and the gas hourly space velocity (GHSV) was maintained at 15,000 mL g_{cat}⁻¹ h⁻¹. Then using the programmable thermal controller raised the bed temperature to 220, 260, and 300 °C, and the catalytic activity was assessed at each temperature. An online gas chromatography (INESA, GC126, China) with a two-column system connected to FID (CH_3OH , CH_4) and TCD (N_2 , CO , CO_2 , CH_4) was used to sample and analyze the outlet gases. CO_2 conversion (X_{CO_2}), CH_3OH selectivity ($S_{\text{CH}_3\text{OH}}$) and CH_3OH space-time yield ($STY_{\text{CH}_3\text{OH}}$) were calculated as follows:

$$X_{\text{CO}_2} (\%) = \frac{[\text{CO}_2]_{\text{in}} - [\text{CO}_2]_{\text{out}}}{[\text{CO}_2]_{\text{in}}} \times 100 \quad (1)$$

$$S_{\text{CH}_3\text{OH}} (\%) = \frac{[\text{CH}_3\text{OH}]_{\text{out}}}{[\text{CO}_2]_{\text{in}} - [\text{CO}_2]_{\text{out}}} \times 100 \quad (2)$$

$$STY_{\text{CH}_3\text{OH}} (\text{mmolCH}_3\text{OH} \cdot \text{h}^{-1} \cdot \text{g}_{\text{cat}}^{-1}) = \frac{F_{\text{CO}_2, \text{in}} \cdot X_{\text{CO}_2} \cdot S_{\text{CH}_3\text{OH}}}{W_{\text{cat}}} \times 100 \quad (3)$$

where $[\text{CO}_2]_{\text{in}}$ and $[\text{CO}_2]_{\text{out}}$ are the amount of CO_2 at the inlet and outlet of the reactor, $[\text{CH}_3\text{OH}]_{\text{out}}$ the amount of CH_3OH at the outlet of the reactor, $F_{\text{CO}_2, \text{in}}$ the molar flow of CO_2 at the inlet of the reactor, and W_{cat} the used catalyst weight. Furthermore, the selectivities of CO and CH_4

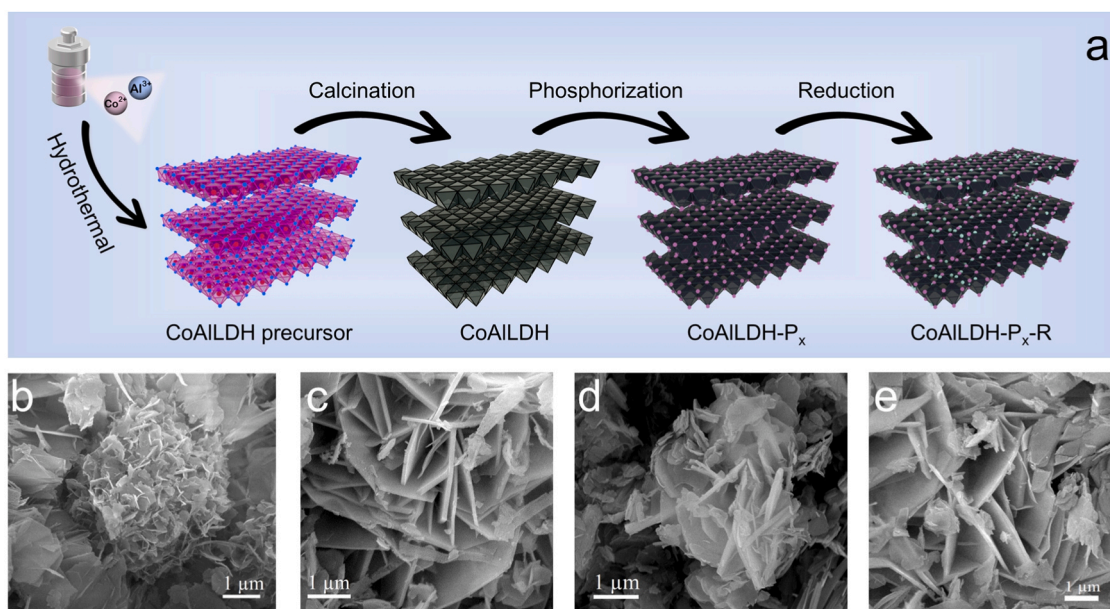


Fig. 1. (a) Schematic illustration of the preparation of CoAILDH-P_x-R; SEM images of (b) CoAILDH precursor, (c) CoAILDH, (d) CoAILDH-P₂, and (e) CoAILDH-P₂-R.

were obtained using similar Eq. (2). In the outlet gases, the carbon-containing products detected were only CO, CH₄, and CH₃OH, so the carbon balance can be calculated by considering CO₂ and the above three products.

2.3. Characterization and DFT calculation

N₂ adsorption-desorption isotherms of the samples were measured at −196.15 °C on an ASAP2460 analyzer. Before the measurement, all the samples were outgassed for 8 h at 120 °C under a high vacuum. A Rigaku Ultima IV X-ray diffractometer operated at 40 kV and 40 mA with Cu Kα irradiation ($\lambda = 0.15406$ nm) was used to record the X-ray diffraction (XRD) patterns of the samples. The phase was identified by comparing it to the Joint Committee on Powder Diffraction Standards (JCPDSs). A Horiba HR Evolution Raman spectrometer with a 532 nm laser as the excitation source was used to record the Raman spectra of the samples in ambient conditions. The spectra ranged from 100 to 1000 cm^{−1}, with a resolution of 1 cm^{−1}. Extended X-ray absorption fine structure (EXAFS) analysis was performed in transmission mode using an easyXAFS300 spectrometer. The instrument was based on Rowland circle geometries with spherically bent crystal analyzers (SBCAs) and an AXAS-M1 silicon drift detector (SDD). High resolution scanning electron microscopy (SEM) with energy-dispersive spectrometry (EDS) was used to characterize the morphologies and elemental analysis of the prepared samples on FEI Inspect F50. The morphologies and structural features of samples were analyzed by transmission electron microscopy (TEM), high-resolution transmission electron microscopy (HRTEM), selected area electron diffraction (SAED), and energy dispersive X-ray (EDX) mapping characterization on a Talos F200X field emission electron microscope operated at an accelerating voltage of 200 kV. X-ray photoelectron spectroscopy (XPS) analysis was conducted on a Thermo Scientific K-Alpha equipped with an Al Kα source ($h\nu = 1486.6$ eV). The binding energy of all elements was calibrated with C 1s peak (284.8 eV) as a reference. The reducibility of the samples was tested by temperature programmed reduction of hydrogen (H₂-TPR) using an AUTO CHEM 2920 chemisorption analyzer. Prior to the measurement, 0.1 g sample was pretreated for 1 h at 200 °C in He flow. After the sample was cooled to 50 °C, the profile was recorded by passing a 10 vol% H₂/He mixture (50 mL/min) across the sample while the temperature was ramped up to 700 °C at a rate of 10 °C/min. Similarly, the CO₂ adsorption capacity of the samples was assessed using CO₂ temperature programmed

desorption (CO₂-TPD) on the same equipment. Firstly, 0.1 g sample was pretreated in He (30 mL/min) at 200 °C for 1 h. After cooled to 50 °C in He, the sample was treated in CO₂ for 2 h to adsorb CO₂, followed by flushing in He for 1 h. The TPD profile was recorded in He flow from 50 °C to 700 °C at a heating rate of 10 °C/min. In-situ diffuse reflectance infrared Fourier transform spectroscopy (DRIFTS) experiment was performed on a Bruker Vertex 80 FT-IR spectrometer equipped with a liquid-nitrogen-cooled MCT detector and a high-temperature reaction cell. A 0.2 g sample was placed in the in-situ cell and pretreated at 200 °C for 1 h in an Ar flow (20 mL/min). Subsequently, it was heated to 300 °C to collect the background spectrum in the range of 800–2000 cm^{−1} at a resolution of 4 cm^{−1} by accumulating 64 scans. Then the test temperature was fixed at 300 °C, but the test gas composition changed in the test process. Initially, pure CO₂ flow (5 mL/min) was constantly supplied into the in-situ cell for 30 min, and the spectra were collected every 5 min. Afterward, H₂ (15 mL/min) was also incorporated without closing the CO₂ gas flow (5 mL/min) for 60 min, and the spectra were collected every 10 min. Finally, the CO₂ gas flow was shut and the H₂ gas flow (15 mL/min) was retained for 30 min, and the spectra were collected every 5 min. The Cambridge Serial Total Energy Package (CASTEP) module carried out the DFT calculation, and the calculation details were provided in Text S2.

3. Results and discussion

3.1. Morphology, phase and textural properties

The CoAILDH precursor with the Co/Al molar ratio of 2:1 was first prepared by hydrothermal method. According to the XRD pattern in Fig. S2, strong reflection peaks of LDH, such as intense and symmetric reflections for (003), (006), and (012) lattice planes at 11.6°, 23.5°, and 34.5°, broad reflections for (015) and (018) lattice planes at 39.2° and 46.7°, and the reflections of (110) and (113) lattice planes at higher 2θ angles, can be identified, which indicates the successful preparation of the layered double hydroxide precursor [17,20,34]. In Fig. 1b, the SEM image of the CoAILDH precursor exhibits a typical flower-like nanosheet structure, which again demonstrates the formation of a typical structure of the layered double hydroxide. After calcination, the complete layered structure is preserved in Fig. 1c. Furthermore, even after phosphating treatment and subsequent reduction, apparent layered structure can be still observed in Figs. 1d and 1e. For CoAILDH-P₂-R, the mass fraction of

the P element is 1.67% as shown by EDS in Fig. S3, which suggests the P element is successfully introduced on the catalyst. In addition, SEM mapping in Fig. S3 further confirms that moderate phosphating can enable the uniform incorporation of phosphorus without damaging the layered structure of the catalyst.

XRD patterns of CoAILDH-R and CoAILDH-P_x-R are shown in Fig. 2a. There is no diffraction peak of alumina, which may be attributed to the fact that alumina is amorphous. For CoAILDH-R, the characteristic peaks at 31.4°, 36.9°, 44.8°, 59.4°, and 65.2° can be indexed well to the (220), (311), (400), (511), and (440) facets of cubic Co₃O₄ (PDF # 78–1970).

All of these peaks are also present in XRD patterns of CoAILDH-P₁-R and CoAILDH-P₂-R, though their diffraction intensities decrease slightly. With the further increase of phosphating degree, a new characteristic peak appears at 43.2° in CoAILDH-P₃-R and CoAILDH-P₄-R, which corresponds to the (211) facet of Co₂P (PDF # 89–3030). The corresponding locally enlarged view in Fig. 2b distinctly illustrates the weakening of Co₃O₄ peaks and even the appearance of Co₂P peaks with the increase of phosphating degree. In addition, there are no CoO and metal Co phases in these reduced samples, indicating CoAILDH and CoAILDH-P_x maintain the excellent stability of LDH. Actually, the formation of Co₂P is

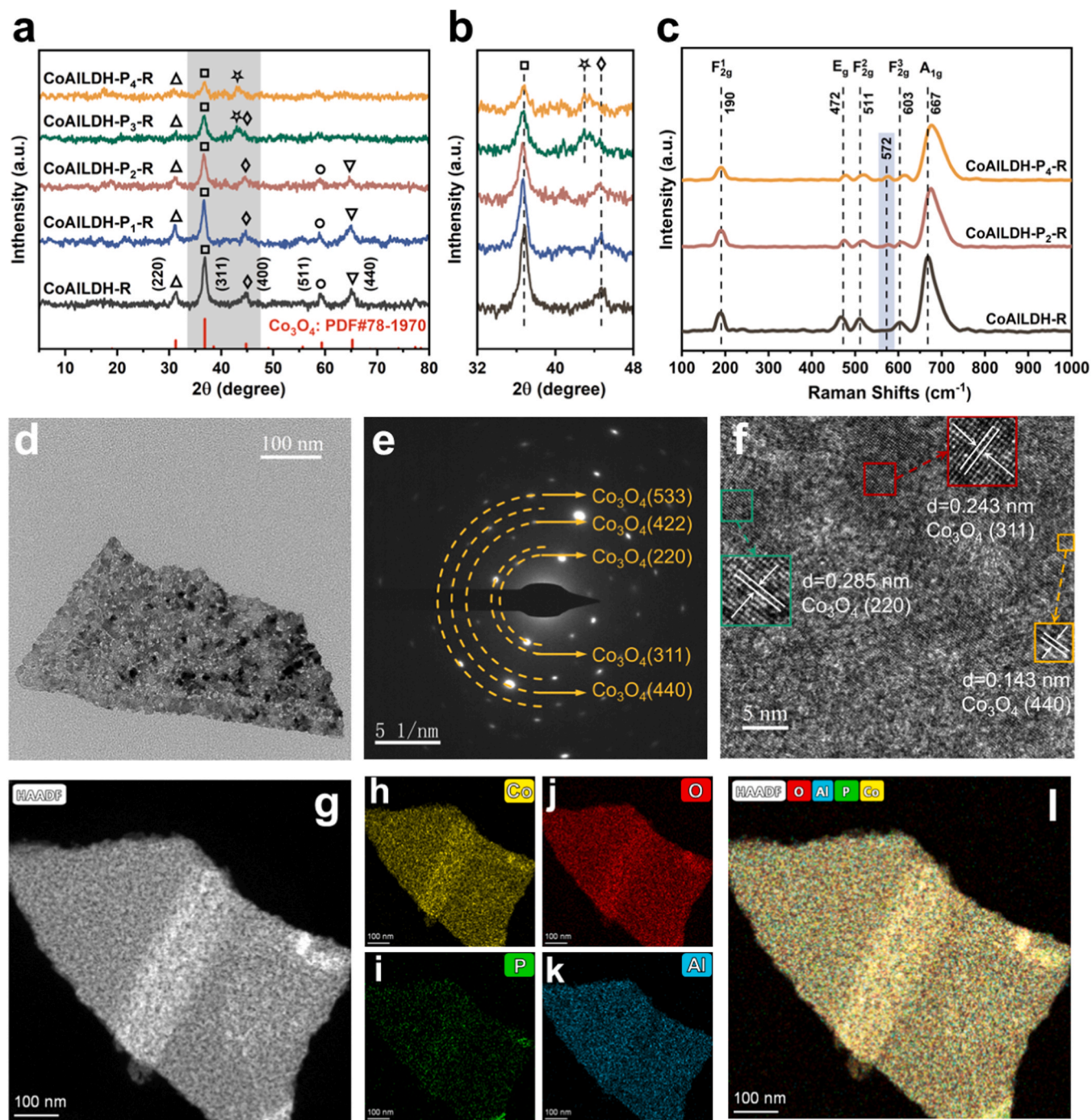


Fig. 2. (a) XRD patterns of CoAILDH-R, CoAILDH-P₁-R, CoAILDH-P₂-R, CoAILDH-P₃-R, and CoAILDH-P₄-R: (Δ) Co₃O₄ (220), (□) Co₃O₄ (311), (◇) Co₃O₄ (400), (○) Co₃O₄ (511), (▽) Co₃O₄ (440), and (☆) Co₂P (211); (b) Enlarged view of XRD patterns within 2θ = 32°–48°; (c) Visible Raman spectra of CoAILDH-R, CoAILDH-P₂-R, and CoAILDH-P₄-R; (d) TEM image, (e) SAED pattern, and (f) HRTEM image of CoAILDH-P₂-R; (g) High-angle annular dark-field image, and (h–l) corresponding EDX mapping of CoAILDH-P₂-R.

attributed to the reaction of abundant PH_3 produced by the thermal decomposition of sodium hypophosphite with surface Co_3O_4 of samples during the phosphating process [30]. Notably, these XRD patterns of the reduced samples are similar to those of the unreduced samples in Fig. S4, indicating that the change in the crystal structures of the samples only occurs in the phosphating process, while the subsequent reduction has no significant effect on their crystal structures.

Raman spectroscopy was performed to further investigate the catalyst crystalline phase structure and the coordination environment of cobalt ions, and the results are shown in Fig. 2c and S5a. Typically, there are five Raman bands centered at around 190, 472, 511, 603, and 667 cm^{-1} , which correspond to the various modes of Co_3O_4 crystal. Accordingly, the band at 190 cm^{-1} is attributed to tetrahedral site characteristics (CoO_4), which is consistent with F_{2g}^1 symmetry. The Raman peaks at 472, 511, and 603 cm^{-1} are corresponding to the E_g , F_{2g}^2 , and F_{2g}^3 symmetries, respectively. Moreover, the band at 667 cm^{-1} originates from the characteristics of octahedral sites (CoO_6), which is related to the A_{1g} species in the Oh^7 spectroscopic symmetry [35,36]. The presence of the Raman bands for the five Co_3O_4 crystallization modes in these catalysts, as shown in Fig. 2c and S5a, indicates that phosphating and subsequent reduction do not cause the Co_3O_4 crystal structure to vanish. However, the Raman peaks of Co_3O_4 in CoAILDH- P_2 -R and CoAILDH- P_4 -R (or, CoAILDH- P_2 and CoAILDH- P_4) are lower, wider, and slightly shift, compared with CoAILDH-R (or, CoAILDH), especially the peaks of F_{2g}^2 , F_{2g}^3 , and A_{1g} . These imply that after phosphating, the original coordination environment of cobalt ions in the crystal changes, which is closely related to the surface charge transfer [35], discussed below. Notably, there is a new peak at about 572 cm^{-1} for CoAILDH- P_x and CoAILDH- P_x -R, and its intensity increases significantly with the degree of phosphating, which is assigned to the characteristic stretching modes of Co-P [37]. Besides, no other vibration peaks can be found, indicating that no other crystalline phases occur in the samples. Further, the coordination environments of CoAILDH-R, CoAILDH- P_2 -R, and CoAILDH- P_4 -R were confirmed by extended X-ray absorption fine structure (EXAFS) spectra. Fig. S5b shows that the Co-O distance of 1.42 Å and the Co-Co distance of 2.45 Å in CoAILDH-R, CoAILDH- P_2 -R, and CoAILDH- P_4 -R correspond to those of Co_3O_4 [22, 35]. And the Co-O and Co-Co distances are shorter than those of CoO, again indicating that Co_3O_4 can maintain stability in these catalysts and the subsequent reduction does not result in CoO crystal production. Importantly, distinguished from CoAILDH-R, a new peak appears at 1.92 Å in CoAILDH- P_2 -R and CoAILDH- P_4 -R, which can be ascribed to Co-P [33], again suggesting that P can be introduced into these catalysts with a controlled degree of phosphating. Combined with the XRD, Raman, and EXAFS results, it is precisely deduced that more P atoms enter the lattice to interact with Co ions during the phosphating process, which promotes the formation of new Co_2P crystalline phase. Moreover, in Fig. S5a, the Raman bands of the reduced samples do not change apparently compared with the unreduced samples, illustrating again that CoAILDH and CoAILDH- P_x catalysts maintain their stable structures during reduction, which is in line with the SEM and XRD results.

To further investigate the morphologies and nanostructures of CoAILDH-R and CoAILDH- P_x -R, TEM characterization was performed. A layered structure with abundant disordered mesopores can be observed in the TEM images of both CoAILDH-R (Fig. S6a) and CoAILDH- P_2 -R (Fig. 2d) [32]. Furthermore, as shown in Fig. S7, the BET specific surface areas of CoAILDH-R and CoAILDH- P_2 -R are 77 and 62 m^2g^{-1} , and the corresponding mean pore sizes are 11.3 and 10.6 nm, respectively. These indicate that the moderate phosphating does not severely damage the catalyst structure and does not cause severe pore collapse and surface reduction. Besides maintaining its morphology, the crystal structure of CoAILDH- P_2 -R is also well preserved after moderate phosphating, as shown by its SAED and HRTEM features when compared to CoAILDH-R. The clear diffraction rings exhibited in Fig. 2e and S6b confirm the excellent crystallite of catalysts [30], with different diffraction rings corresponding to different crystal faces of Co_3O_4 . Likewise, Fig. 2f and

S6c present the HRTEM images of the local region of catalysts, where the lattice fringes with the spacing of 0.143, 0.243, and 0.285 nm can correspond to the (440), (311), and (220) facets of Co_3O_4 , respectively. These results again prove that the original morphology and crystal structure of catalysts can be well maintained after moderate phosphating treatment. Also, Fig. 2g-l show that Co, P, O, and Al are uniformly distributed throughout CoAILDH- P_2 -R, confirming that phosphorus element can not only be successfully introduced into the catalyst but also dispersed uniformly during the phosphating treatment. In Fig. S8, the EDX spectrum and the corresponding elemental contents manifest that the mass fraction of phosphorus is 1.8%, close to the EDS result, again proving that P is distributed very uniformly in CoAILDH- P_2 -R. In comparison with CoAILDH- P_2 -R, CoAILDH- P_4 -R also has a layered morphology and similar crystal structure (Figs. S9a-c), but the EDX results (Figs. S9d-j) show that the content of P is 1.6%. As for CoAILDH- P_4 -R, although it still retains a favorable layered morphology (Fig. S10a), excessive phosphating leads to a change in its crystal structure (Figs. S10b-c). Specifically, as the uniformly distributed P content increases to 3.8%, in addition to the crystal plane of Co_3O_4 , the (211) facet of Co_2P appears in the SAED pattern of CoAILDH- P_4 -R (Figs. S10b-j). Therefore, the phosphating degree of the catalysts can be controlled during the preparation, and the CoAILDH- P_2 -R with moderate phosphating can not only achieve uniform incorporation of plentiful P elements but also prevent the generation of the new crystalline phase.

3.2. Surface properties

Typically, the surface chemical state of elements on the catalysts greatly affects CO_2 adsorption and hydrogenation. To examine the surface chemical state of Co, P, Al, and O species of the as-prepared catalysts, an XPS test was carried out. Fig. S11 illustrates the XPS measurement spectra, from which the characteristic peaks of the P species can be identified. The obvious peak intensity change can be seen from the locally enlarged views, further indicating that the P element can be successfully introduced into the catalysts by phosphating treatment and the degree of phosphating can be controlled. As shown in Fig. 3a, all samples exhibit the typical asymmetric Co 2 $p_{3/2}$ and Co 2 $p_{1/2}$ satellite peaks at the binding energies of 786.1, 789.2, 801.9, and 804.5 eV, respectively, by the split-peak fitting. It indicates that Co species in the samples mainly exist as Co_3O_4 [27,38], which matches well with the XRD, Raman, and EXAFS results. Although Co_3O_4 exhibits special crystal structure and properties, it can be approximated as a compound of cobalt oxide (CoO) and cobaltic oxide (Co_2O_3), and thus the cobalt in Co_3O_4 has both +2 and +3 valences [31]. Two peaks at about 780.2 and 795.4 eV are associated with Co^{3+} , and two peaks at about 781.6 and 797.1 eV belong to Co^{2+} , suggesting the co-existence of Co^{2+} and Co^{3+} in the catalysts. It is worth noting that there are another two peaks that appear at 776.9 and 791.3 eV, which can be ascribed to the Co^{6+} in the Co-P bonds formed following excessive phosphating [31, 39]. Besides, with the increase of phosphating degree, in addition to the obvious decrease of the proportion of Co^{3+} , the binding energy of each peak of the Co 2p orbital has a certain degree of decrease, which is due to the electron transfer on the catalyst surface caused by the P modification [30]. When compared with the Co 2p core spectra of the unreduced catalysts in Fig. S12a, only the proportion of Co^{3+} shows a slight decrease after reduction, again confirming the favorable stability of the catalysts.

Figs. S12b and 3b show the core level spectra of P 2p in the samples before and after reduction, in which the predominant peak at around 133.6 eV after the split-peak fitting can be assigned to the P-O [39]. Also, there are two peaks with the binding energy of 129.5 and 130.8 eV that can be attributed to the Co-P bond in P 2 $p_{3/2}$ and P 2 $p_{1/2}$, which further supports the existence of the Co-P bond in the surface structure of the phosphide catalysts [31]. Similarly, due to the excellent stability of the catalysts, there is no apparent variation in the peaks of the P 2p core level spectra before (Fig. S12b) and after (Fig. 3b) reduction.

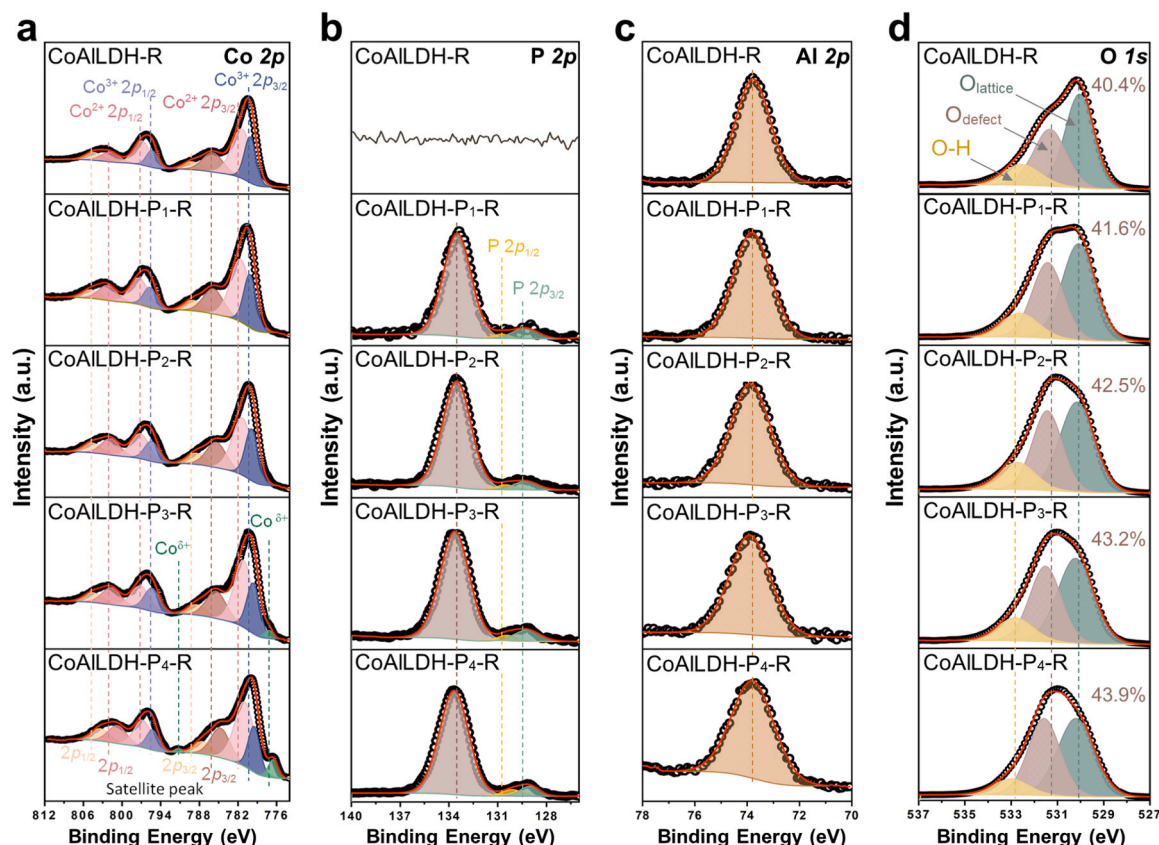


Fig. 3. XPS spectra of (a) Co 2p, (b) P 2p, (c) Al 2p, and (d) O 1s of CoAlLDH-R, CoAlLDH-P₁-R, CoAlLDH-P₂-R, CoAlLDH-P₃-R, and CoAlLDH-P₄-R.

Importantly, as the P content increases, the binding energy of peaks attributed to Co-P gradually decreases, indicating an increase in the electron density around P [30]. Furthermore, the core energy level spectra of Al 2p of the samples reveal that neither phosphating treatment (Fig. S12c) nor subsequent reduction (Fig. 3c) has any discernible influence on its binding energy and peak, demonstrating the excellent stability of Al, which is considered to be one of the key reasons for the catalyst stability [26].

Fig. 3d and S12d depict the core level spectra of O 1s. Following deconvolution, three peaks can be clearly visible at about 530.1, 531.3, and 532.9 eV, corresponding to lattice oxygen (O_{lattice}), oxygen vacancies (O_{defect}), and a small amount of OH species adsorbed on the surface, respectively [16,40]. Typically, the peak areas (A) of O_{lattice} and O_{defect} can be used to assess the density of oxygen vacancies ($C_{O_{\text{defect}}}$) using the formula $C_{O_{\text{defect}}} = A_{O_{\text{defect}}} / (A_{O_{\text{defect}}} + A_{O_{\text{lattice}}}) \times 100\%$ [17,22]. According to Fig. S12d, the values of $C_{O_{\text{defect}}}$ are 39.3%, 40.8%, 41.9%, 42.9% and 43.6% for CoAlLDH, CoAlLDH-P₁, CoAlLDH-P₂, CoAlLDH-P₃, and CoAlLDH-P₄, respectively. According to Fig. 3d, the $C_{O_{\text{defect}}}$ values are 40.4%, 41.6%, 42.5%, 43.2% and 43.9% for CoAlLDH-R, CoAlLDH-P₁-R, CoAlLDH-P₂-R, CoAlLDH-P₃-R and CoAlLDH-P₄-R, respectively. Apparently, $C_{O_{\text{defect}}}$ increases very slightly not only with the phosphating degree but also after reduction, and the effects of both phosphating and reduction on the concentration of oxygen vacancies are basically negligible. Importantly, as shown in Fig. 3d and S12d, the binding energy attributed to the oxygen vacancy exhibits a certain increasing trend with the increase of phosphating degree, again demonstrating that there is a significant electron transfer on the surface of the catalysts, that is, the abundant electrons in the oxygen vacancy transfer toward the surrounding atoms. It is worthwhile to note that the electron transfer on the surface of the catalysts would inevitably affect the dissociation of H₂ on the active sites and the adsorption and hydrogenation of CO₂, as discussed in detail below.

3.3. Reduction and adsorption properties

As stated above, although the phosphating treatment has an impact on the catalyst crystal structure, neither the crystal structure of CoAlLDH nor that of CoAlLDH-P_x has a significant change after the reduction at 300 °C. Thus, to further clarify the structural changes of each catalyst in the reduction process and the effect of phosphating treatment on the reduction behavior, the H₂-TPR characterization was conducted. Typically, bulk Co₃O₄ has two reduction peaks, one peak at the lower temperature representing the reduction of Co₃O₄ to CoO and another peak at the higher temperature assigning to the reduction of CoO to Co [17]. Because Co ions can interact with nearby groups through Co-O bonds and thereby be polarized by Al³⁺ in metal oxides, which hinders the reduction of cobalt species, the number of Al³⁺ around Co ions primarily determines the reduction temperature of the surface species and the crystalline [23,41]. As shown in Fig. 4a, for CoAlLDH, the first small peak centered at 315 °C can be ascribed to the reduction of partial surface Co³⁺ species, while the second peak at 492 °C is attributed to the reduction of Co³⁺ in the bulk phase. The last peak centered at 680 °C is attributed to the reduction of CoO to Co⁰, which possibly also includes the reduction of Co²⁺ in amorphous CoAl₂O₄ [25], although the characteristic peaks for spinel are not detected by XRD. After phosphating, P elements are introduced into the catalysts, which gradually destroys the structure of surface Co₃O₄ and causes its reduction peak to disappear. And the reduction of bulk Co³⁺ is also obviously limited and its reduction temperature increases to about 559 °C. In addition, all the reduction peak areas are reduced after phosphating. Especially for CoAlLDH-P₃ and CoAlLDH-P₄, the excessive phosphating leads to the formation of irreducible Co₂P [42].

In Fig. 4b, CO₂-TPD directly reflects the adsorption capacity of the prepared catalysts for CO₂. For all samples, the peak denoted as α is centered at around 92 °C, which can be attributed to the desorption of

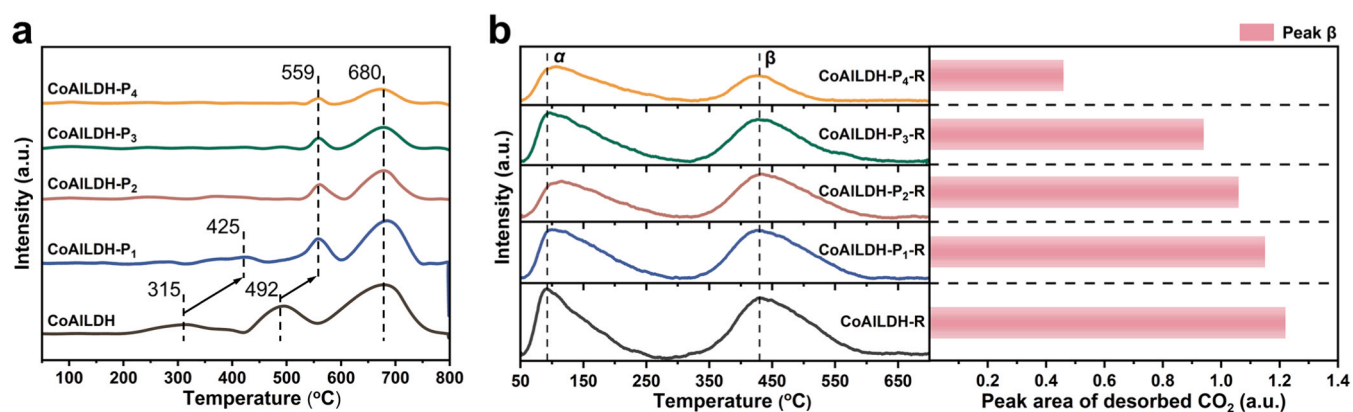


Fig. 4. (a) H₂-TPR profiles of calcined CoAILDH, CoAILDH-P₁, CoAILDH-P₂, CoAILDH-P₃, and CoAILDH-P₄; (b) CO₂-TPD profiles of CoAILDH-R, CoAILDH-P₁-R, CoAILDH-P₂-R, CoAILDH-P₃-R, and CoAILDH-P₄-R, and the corresponding peak areas of the desorbed CO₂.

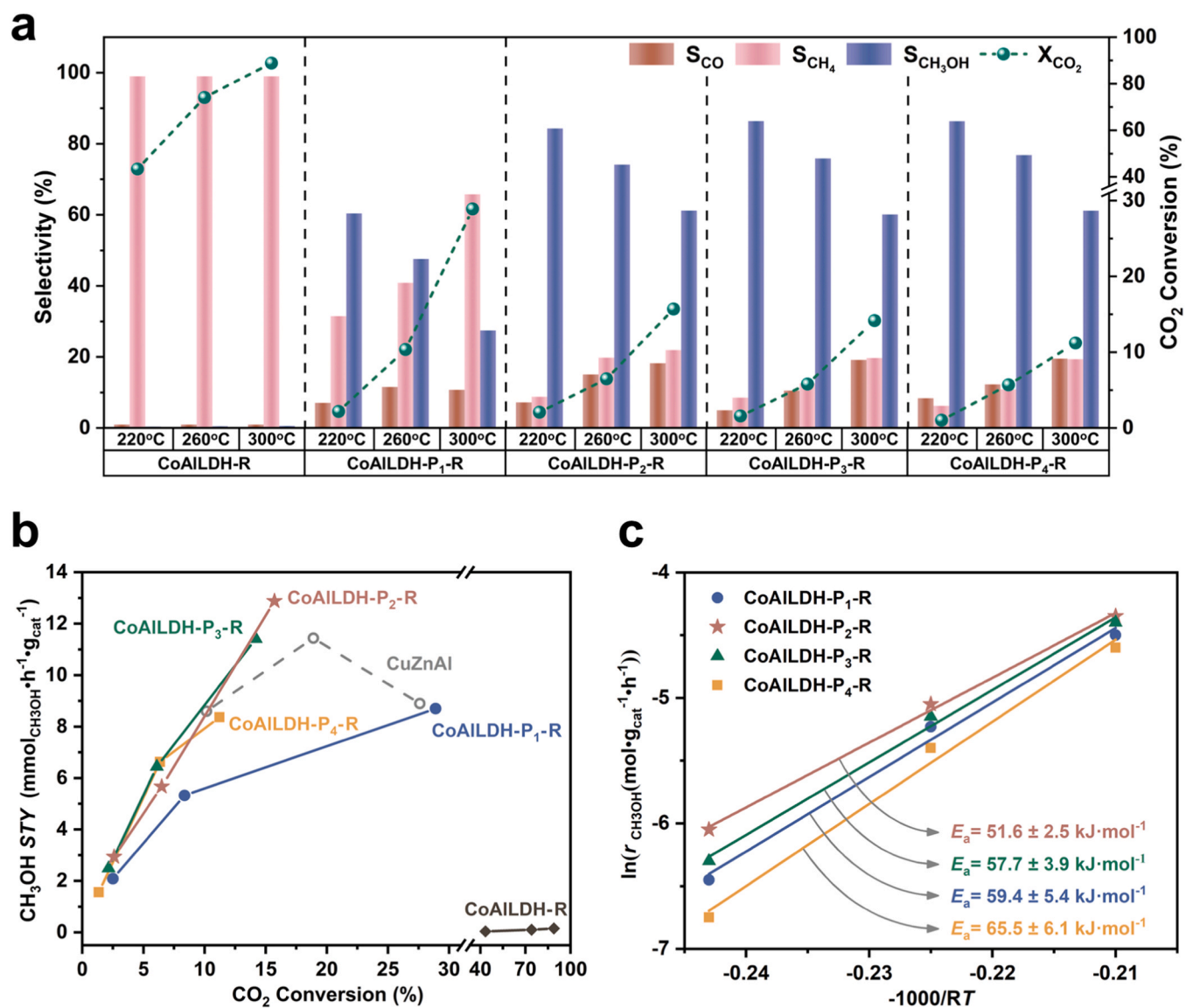


Fig. 5. (a) Catalytic performance of CoAILDH-R, CoAILDH-P₁-R, CoAILDH-P₂-R, CoAILDH-P₃-R, and CoAILDH-P₄-R; (b) CO₂ conversion versus CH₃OH STY of these catalysts at 220–300 °C; (c) Arrhenius plots for methanol formation over CoAILDH-P₁-R, CoAILDH-P₂-R, CoAILDH-P₃-R, and CoAILDH-P₄-R.

the physically adsorbed CO₂ as well as the CO₂ desorption generated from the removal of hydroxyl groups by the decomposition of bicarbonates adsorbed on the catalyst surface [23,43]. The other peak denoted as β is located between 300 and 650 °C, which belongs to the CO₂ arising from the decomposition of carbonates adsorbed at the oxygen vacancies [44,45]. It is these relatively stable adsorbed carbonates that undergo the hydrogenation and conversion to form different products. It is worth noting that the decreasing area of the β peak shows that as the degree of phosphating increases, the capacity of CO₂ adsorption on the catalyst surface gradually declines. This is mainly attributed to the alteration in the property of oxygen vacancies induced by phosphating, that is, the introduction of phosphorus leads to the transfer of electrons in surface oxygen vacancies, which has a negative effect on CO₂ adsorption. Furthermore, as depicted in Figs. 2a and 2b, after excessive phosphating, the Co₂P crystal is formed in CoAILDH-P₃-R and CoAILDH-P₄-R. The new phase is very unfavorable for CO₂ adsorption, which will be discussed in detail below.

3.4. Catalytic performance

All catalytic tests in this work were conducted using catalysts with a mesh size of 20–40, and preliminary measurements show negligible internal diffusion resistance. The carbon balance was above 97% in all the tests. Fig. 5a displays the CO₂ hydrogenation performance of various catalysts after reduction at 300 °C. Despite possessing an 88.9% CO₂ conversion at 300 °C, CoAILDH-R is 98.1% selective for methane, and the reaction products contain trace amounts of methanol. However, after phosphating, methane is restrained greatly and methanol is produced selectively. At any reaction temperature, the methanol selectivity firstly increases noticeably with increasing the phosphating degree, and then tends to be stable from the beginning of CoAILDH-P₂-R. For instance, selectivities to methanol are 27.5% for CoAILDH-P₁-R, 61.1% for CoAILDH-P₂-R, 60.5% for CoAILDH-P₃-R, and 61.2% for CoAILDH-P₄-R, respectively, at the reaction temperature of 300 °C. In conjunction with the previous characterization, the electron transfer at the active sites as well as the change in the catalyst surface structure indeed affects the CO₂ hydrogenation path, resulting in a considerable change in the selectivities of the products. On the other hand, at any reaction temperature, the CO₂ conversion is greatly lowered after phosphating and further decreases with increasing the degree of phosphating, due to the decrease in CO₂ adsorption capacity shown in Fig. 4b. The CO₂ conversions of CoAILDH-P₁-R, CoAILDH-P₂-R, CoAILDH-P₃-R, and CoAILDH-P₄-R are 28.9%, 15.7%, 14.2%, and 11.2% at 300 °C, respectively.

As shown in Fig. 5b, after phosphating, although the CO₂ conversion is reduced, the methanol STY is significantly improved. It follows that the hydrogenation path of CO₂ on the surface of the phosphide catalysts is greatly distinct from that on CoAILDH-R. Fig. S13a also demonstrates the variation of CH₃OH STY of these catalysts with reaction temperature. Among the four phosphide catalysts, CoAILDH-P₂-R exhibits the best methanol STY, which can reach a maximum of 12.9 mmol_{CH₃OH}·h⁻¹·g_{cat}⁻¹ in the examined range of reaction conditions. Remarkably, it exceeds the methanol STY of the conventional CuZnAl catalyst on the same experimental equipment. Moreover, the apparent activation energies of the phosphide catalysts for methanol formation are assessed using the Arrhenius formula. Here, in terms of CH₃OH STY, the methanol formation rate is estimated for each catalyst and each reaction temperature [17,44], and then Arrhenius behaviors are plotted in Fig. 5c. It is found that CoAILDH-P₂-R has the lowest apparent activation energy, and thus it can efficiently lower the energy barrier for methanol formation.

By adjusting the gas hourly space velocity (GHSV), the performance of CoAILDH-P₂-R was further investigated. In Fig. S13b, both the CO₂ conversion and the CH₃OH selectivity remain almost constant, while the methanol STY as expected increases with the increase of GHSV and it can reach 17.3 mmol_{CH₃OH}·h⁻¹·g_{cat}⁻¹ at the GHSV of 20000 mL·g_{cat}⁻¹·h⁻¹. To further test the performance of CoAILDH-P₂-R, the catalytic stability

experiment was performed. As shown in Fig. S13c, the catalyst maintains excellent stability during the long-term test, indicating that the structure of the active sites can remain stable during the methanol synthesis process. Furthermore, CoAILDH-P₂-R has great performance advantages over some Cu-based, In₂O₃-based, and noble metal-based catalysts that have been reported to be suitable for the hydrogenation of CO₂ to methanol, as seen in Table S1. Also, Cu-based catalysts are easy to agglomerate and inactivate after long-term operation [8,10], In₂O₃-based catalysts can be reduced and destroyed during hydrogenation reaction [15], and noble metal-based catalysts are expensive. Compared with these usual catalysts, CoAILDH-P₂-R has higher catalytic performance, more excellent stability, and more reasonable cost. Therefore, the catalyst holds considerable promise for commercial application in the hydrogenation of CO₂ to methanol. It should be mentioned that the selectivity of CH₄ in the product is still more than 10% (Fig. 5a), and thus CoAILDH-P₂-R can be further optimized in the subsequent work, especially to further improve the selectivity of methanol.

3.5. Reaction mechanism and discussion

In order to reveal the cause of the conversion of CO₂ to methanol on the catalyst surface, the reaction mechanism and the structural evolution of CO₂ hydrogenation intermediates were systematically investigated by combining in-situ DRIFTS with DFT calculations. Fig. 6a–c and S14 correspond to the DRIFTS spectra recorded in the range of 800–2000 cm⁻¹ over CoAILDH-P₂-R and CoAILDH-R when switching different transient conditions at 300 °C, respectively. In pure CO₂, the peaks at 1324 and 1534 cm⁻¹ (Fig. 6a) or at 1321 and 1517 cm⁻¹ (Fig. S14a) are attributed to carbonates. As shown in Fig. S15, the amount of these carbonate species adsorbed on CoAILDH-P₂-R (Fig. 6a) and CoAILDH-R (Fig. S14a) tends to be stable over time after a gradual increase [8,43]. Furthermore, it is also demonstrated that CoAILDH-R has a better CO₂ adsorption capacity than CoAILDH-P₂-R, which is in line with CO₂-TPD.

After that, hydrogen was injected into the quartz pool to achieve a ratio of CO₂ to H₂ of 1:3, and the DRIFTS spectra continued to be traced. Due to the hydrogenation of CO₂ by the attack of reactive H* generated by the cleavage of H₂, the concentration of CO₃* gradually decreases and then reaches equilibrium (Figs. 6b, S14b, and 6d). As such, new vibrational bands appear at 1385 and 1607 cm⁻¹ (Fig. 6b) or at 1369 and 1591 cm⁻¹ (Fig. S14b) and gradually increase over time, resulting from the C-H stretching mode and O-C-O bending mode generated in the formate (HCOO*) intermediate [9,46]. Meanwhile, a vibration band at 1075 cm⁻¹ (Fig. 6b) or 1068 cm⁻¹ (Fig. S14b) is observed, which can be assigned to the stretching vibration of C-O in another key intermediate methoxy species (H₃CO*) [16,17]. It is important to note that the content of H₃CO* on the surface of CoAILDH-P₂-R is close to that on CoAILDH-R (Fig. 6f), even though the contents of intermediate CO₃* and HCOO* on the surface of CoAILDH-R are substantially higher than those on CoAILDH-P₂-R (Fig. 6d–e). It further indicates that the consumption rate of H₃CO* on CoAILDH-P₂-R is significantly lower than that on CoAILDH-R, leading to the accumulation of H₃CO* on the surface of CoAILDH-P₂-R, which may be because the breaking of the C-O bond in H₃CO* is constrained on the surface of CoAILDH-P₂-R. In addition, the appearance of the vibration band attributed to COOH* at 1703 cm⁻¹ also suggests that the hydrogenation path of CO₂ on CoAILDH-P₂-R has changed considerably compared with CoAILDH-R [17]. After the flow of CO₂ is turned off, all these vibration bands belonging to intermediates on CoAILDH-P₂-R (Fig. 6c) and CoAILDH-R (Fig. S14c) can be observed to gradually weaken and even disappear, indicating that the intermediates accumulated on the catalyst surface can be entirely activated by sufficient H*. Moreover, in-situ DRIFTS spectra in the range of 2800–3100 cm⁻¹ over CoAILDH-P₂-R and CoAILDH-R are also recorded under CO₂ and H₂ at 300 °C. In Figs. S14d–e, although the vibrational band attributed to HCOO* is observed on both catalysts, the vibrational

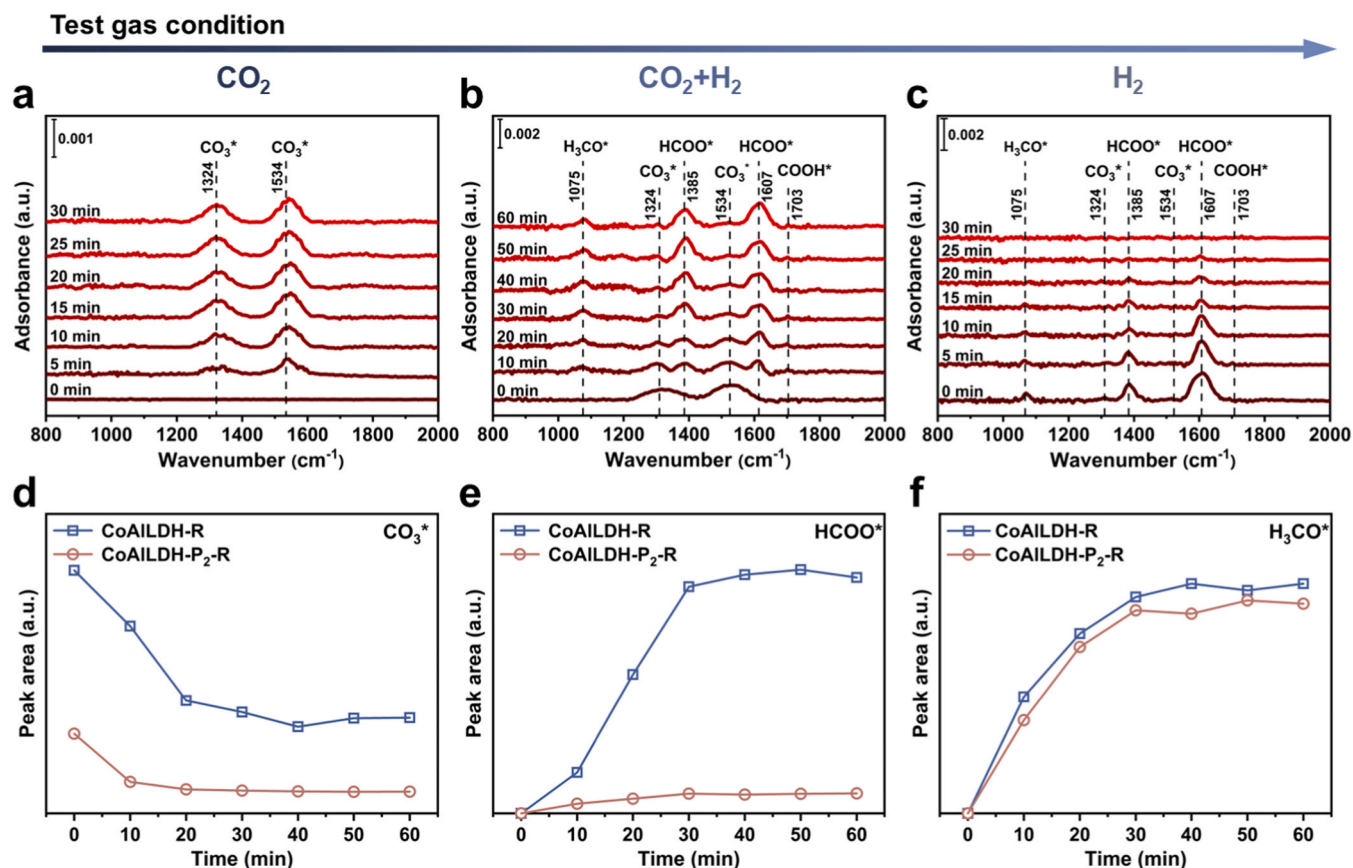


Fig. 6. In-situ DRIFTS spectra over CoAILDH-P₂-R at 300 °C under different gas conditions with continuous switching: (a) CO₂, (b) CO₂ + H₂, and (c) H₂; Comparison of intermediate species of CO₂ hydrogenation over CoAILDH-R and CoAILDH-P₂-R during 60 min: (d) CO₃^{*}, (e) HCOO^{*}, and (f) H₃CO^{*}.

band attributed to the C-H vibrational mode of methane occurs at 3015 cm⁻¹ only on CoAILDH-R [6,44], indicating that methane generation on CoAILDH-P₂-R is significantly inhibited. Based on these experimental phenomena, we deduce that the principal hydrogenation paths of CO₂ adsorbed on the two catalysts are different, causing different predominant products. Specifically, unlike CoAILDH-R on which the C-O bond in H₃CO^{*} is broken and then hydrogenated to methane, more key intermediate H₃CO^{*} prefers direct hydrogenation to methanol on CoAILDH-P₂-R.

Actually, it is not precise enough to deduce the reaction path solely based on in-situ DRIFTS results. To further identify the hydrogenation reaction path of CO₂, isotopic experiments [47,48] or density functional theory (DFT) calculations [8,9,13] can be conducted. In the present work, DFT calculations were performed to further investigate the effect of phosphating modification on the CO₂ hydrogenation path. The CoAILDH-R model is represented by constructing the defective Co₃O₄ (311) surface by removing an oxygen atom from the perfect Co₃O₄ (311) surface. Also, the structure was optimized to represent the CoAILDH-P₂-R model by the defective Co₃O₄ (311) surface modified by a phosphorus atom. In Fig. S16, the density of states (DOS) of CoAILDH-R and CoAILDH-P₂-R indicate that the incorporation of P does not destroy the metallicity of the catalytic material. And the continuous DOS near the Fermi level (*E_f*) indicates that massive electrons can be transferred on the catalyst surface, which helps to accelerate the reaction rate. In particular, the *d*-band center of CoAILDH-R is closer to the Fermi level and thus endows it with stronger adsorption and activation of hydrogen (Fig. 7d) [49,50]. Moreover, Fig. S17 shows the electron density of the atoms around the oxygen vacancy on CoAILDH-P₂-R is lower than that on CoAILDH-R, in good agreement with the above XPS result, which may result in a weaker ability of CoAILDH-P₂-R to adsorb and activate reactants as well as a lower bond strength to the

intermediate [51]. Indeed, the calculation results show that hydrogen can be activated to H^{*} on both catalysts (Fig. S18), but the activation barrier of hydrogen adsorption on CoAILDH-P₂-R (0.61 eV) is higher than that of CoAILDH-R (0.32 eV), indicating that the introduction of P confines the hydrogen adsorption and dissociation. Thus, a weaker H₂ cleavage ability would inevitably lead to a lower H^{*} concentration on the surface of CoAILDH-P₂-R, which could limit the excessive hydrogenation of CO₂ [52]. Besides, in Table S2, the calculated energies for CO₂ adsorption on the CoAILDH-R and CoAILDH-P₂-R models are -0.23 and -0.11 eV, respectively, again proving that the adsorption of CO₂ is limited after P incorporating, in good agreement with CO₂-TPD. Meanwhile, the CO₂ adsorption energy of Co₂P generated by excessive phosphating is 0.36 eV, manifesting that it is not suitable to conduct the CO₂ adsorption and hydrogenation.

Based on the characterization results of the in-situ DRIFTS, the reaction paths of CO₂ hydrogenation were examined on the CoAILDH-R and CoAILDH-P₂-R. And the most likely reaction paths are described in Fig. 7a and S19, with the optimized structures of all the reaction intermediates involved in the two catalysts shown in Figs. S20-S21. As stated above, the CO₂ adsorption capacity of CoAILDH-R is better than that of CoAILDH-P₂-R. The activated CO₂^{*} can be attacked by H^{*} on the surface to generate HCOO^{*} intermediate, which is a thermodynamically favorable process on both CoAILDH-R and CoAILDH-P₂-R but requires crossing 0.47 and 0.60 eV activation energy barriers, respectively. The hydrogenation of HCOO^{*} to H₂COO^{*} is thermodynamically favorable on CoAILDH-R, but it is thermodynamically unfavorable on CoAILDH-P₂-R. The energy barriers to generate H₂COO^{*} on CoAILDH-R and CoAILDH-P₂-R are 0.76 and 0.98 eV, respectively. As stated above, CoAILDH-R has better CO₂ adsorption capacity, and thus the intermediate conversion process on it is more favorable in thermodynamics, which leads to its higher CO₂ conversion. The reaction energy diagrams

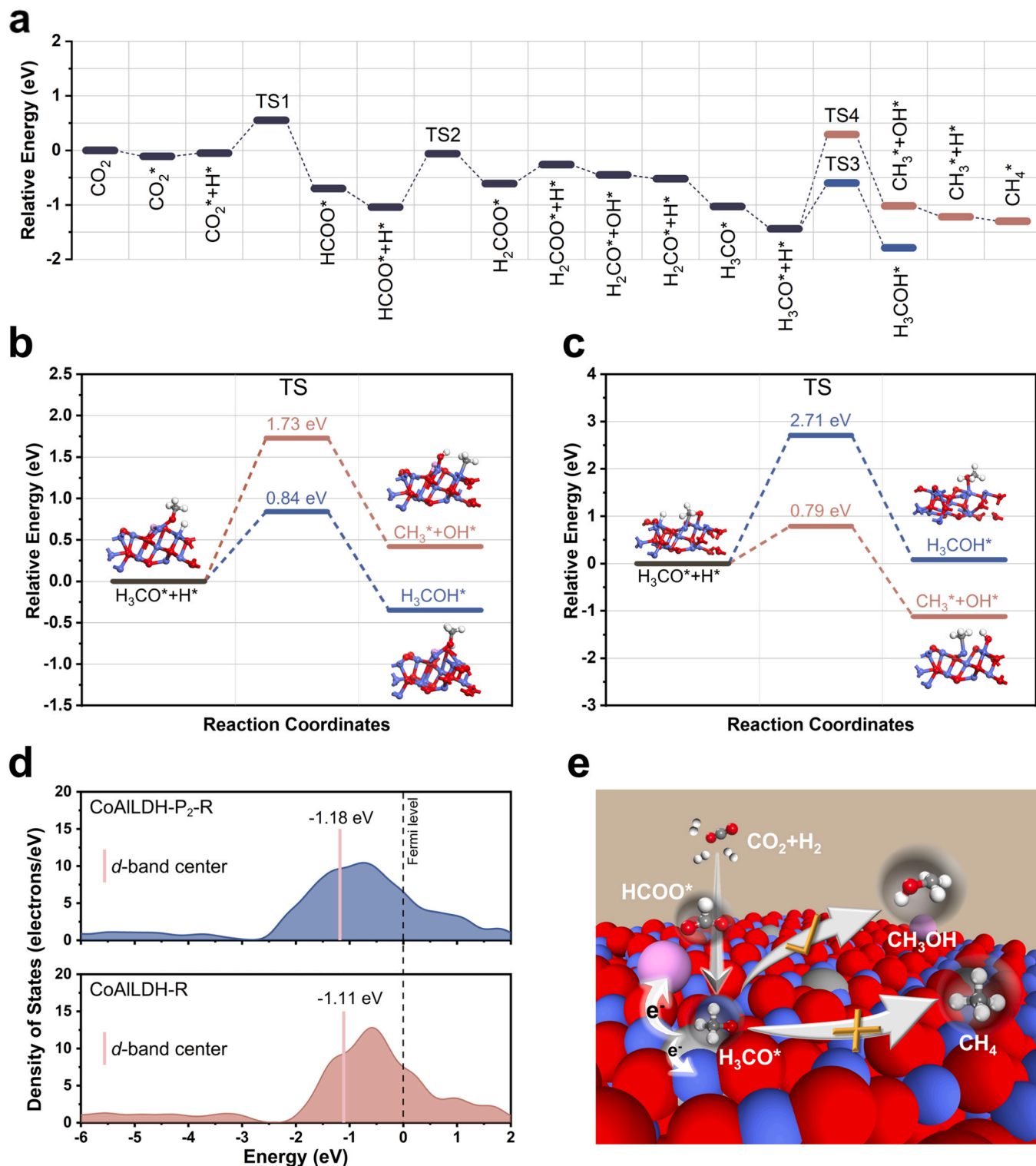


Fig. 7. (a) Reaction energy diagram for CO₂ hydrogenation on the CoAILDH-P₂-R model catalyst; Reaction energy diagram for the hydrogenation routes of H₃CO* over the (b) CoAILDH-P₂-R and (c) CoAILDH-R models; (d) Partial density of states (PDOS) of the atoms near the oxygen vacancy on the surface of the CoAILDH-P₂-R and CoAILDH-R models; (e) Mechanism illustration and CO₂ hydrogenation pathways on CoAILDH-P₂-R; The balls in blue, red, pink, gray, and white represent cobalt, oxygen, phosphorus, carbon, and hydrogen atoms, respectively, while the large light gray ball represent oxygen vacancy.

and corresponding transition state (TS) structures of the formation of HCOO* and H₂COO* can be found in Figs. S22-S23. For both CoAILDH-R and CoAILDH-P₂-R, the subsequent hydrogenation of H₂COO* proceeds via the stepwise formation of H₂CO* and H₃CO*. It follows from Fig. 6 that the following hydrogenation of H₃CO* serves as the dominating factor leading to a difference in the dominated product

on CoAILDH-R and CoAILDH-P₂-R. Specifically, there are two possible paths for the subsequent hydrogenation of the key intermediate H₃CO*: One is direct hydrogenation to H₃COH*, and the other is further hydrogenation to CH₄* from CH₃* formed by C-O cleavage in H₃CO*. As shown in Figs. 7b and 7c, the hydrogenation of H₃CO* to H₃COH* on CoAILDH-P₂-R requires overcoming the activation barrier of 0.84 eV,

which is much lower than that (1.73 eV) for the formation of methyl (CH_3^*) and hydroxyl (OH^*) groups. This illustrates that H_3CO^* on CoALDH-P₂-R tends to hydrogenate directly to form methanol, resulting in a significantly higher selectivity of methanol than methane on the catalyst. On the other hand, the hydrogenation of H_3CO^* to methanol on CoALDH-R is not only a thermochemically unfavorable process, but also demands crossing an energy barrier (2.71 eV) that is substantially higher than that (0.79 eV) encountered in the production of CH_3^* and OH^* , proving that CoALDH-R favors the formation of methane rather than methanol. The specific initial state, transition state (TS), and final state structures of the corresponding H_3CO^* hydrogenation path on the two catalyst models can be found in Fig. S24.

In a word, a preliminary mechanism illustration of CO_2 hydrogenation over CoALDH-P₂-R is shown in Fig. 7e. After phosphating, a uniform P incorporation causes the electron transfer in the oxygen vacancies on the Co_3O_4 crystal surface and thus significantly changes the hydrogenation path of adsorbed CO_2 . The crucial point is to constrain the decomposition and deep-hydrogenation of the key intermediate H_3CO^* to methane, and instead to promote the direct hydrogenation of H_3CO^* to produce more methanol. In addition to improving the methanol selectivity, phosphating exerts a negative effect on H_2 activation and CO_2 adsorption and conversion. Especially, excessive phosphating leads to the formation of the Co_2P crystal which severely inhibits CO_2 adsorption and hydrogenation. Therefore, moderate phosphating showing the high methanol STY is recommended to modify the Co-Al catalyst to boost the CO_2 hydrogenation to methanol.

4. Conclusions

In this work, a stable layered-structure CoALDH catalyst was prepared from layered double hydroxide, and then a phosphating strategy was applied to modify the catalyst surface. Due to the excellent structure of the catalyst, phosphating can achieve a uniform incorporation of P without damaging the original layered morphology. The catalyst crystal structure is preserved after moderate phosphating, but more P introduction promotes the formation of Co_2P after excessive phosphating. Experiments and DFT calculations show that a significant electron transfer occurs after phosphating, that is, electrons in the surface oxygen vacancies transfer toward the surrounding atoms, which restricts the CO_2 adsorption and H_2 activation. Also, the generated Co_2P crystal further inhibits CO_2 adsorption. The CO_2 conversion, therefore, decreases with the degree of phosphating. However, the induced surface electron transfer changes the hydrogenation path of adsorbed CO_2 , and the methanol selectivity and STY are significantly improved after phosphating. Especially, the CoALDH-P₂-R obtained by moderate phosphating shows the highest methanol STY, far superior to conventional Cu-, In_2O_3 - and noble metal-based catalysts. In-situ DRIFTS reveals that the high concentration of key intermediate H_3CO^* is the crucial factor for the massive rise in methanol on the phosphide catalysts. Moreover, DFT discloses that the phosphide catalysts confine the conversion of CO_2 to methane by preventing the C-O bond cleavage in H_3CO^* , but instead facilitate the direct hydrogenation of H_3CO^* to methanol. In summary, this work explores the effect of catalyst phosphating on the CO_2 hydrogenation path, providing a strategy to design and optimize the catalytic active sites to manipulate the reaction path.

CRedit authorship contribution statement

Heng Zhang: Investigation, Methodology, Data curation, Software, Visualization, Writing – original draft. **Donglei Mao:** Data curation, Visualization. **Jinxin Zhang:** Visualization. **Dongfang Wu:** Resources, Investigation, Supervision, Writing – review & editing.

Declaration of Competing Interest

The authors declare that they have no known competing financial

interests or personal relationships that could have appeared to influence the work reported in this paper.

Data Availability

Data will be made available on request.

Acknowledgment

This work was supported by the National Natural Science Foundation of China under Grant No. 21878048.

Appendix A. Supporting information

Supplementary data associated with this article can be found in the online version at doi:10.1016/j.apcatb.2023.123257.

References

- [1] J.W. Zhong, X.F. Yang, Z.L. Wu, B.L. Liang, Y.Q. Huang, T. Zhang, State of the art and perspectives in heterogeneous catalysis of CO_2 hydrogenation to methanol, *Chem. Soc. Rev.* 49 (2020) 1385–1413, <https://doi.org/10.1039/c9cs00614a>.
- [2] X. Jiang, X. Nie, X. Guo, C. Song, J.G. Chen, Recent advances in carbon dioxide hydrogenation to methanol via heterogeneous catalysis, *Chem. Rev.* 120 (2020) 7984–8034, <https://doi.org/10.1021/acs.chemrev.9b00723>.
- [3] O. Geden, Politically informed advice for climate action, *Nat. Geosci.* 11 (2018) 380–383, <https://doi.org/10.1038/s41561-018-0143-3>.
- [4] E.V. Kondratenko, G. Mul, J. Baltrusaitis, G.O. Larrazabal, J. Perez-Ramirez, Status and perspectives of CO_2 conversion into fuels and chemicals by catalytic, photocatalytic and electrocatalytic processes, *Energ. Environ. Sci.* 6 (2013) 3112–3135, <https://doi.org/10.1039/c3ee41272e>.
- [5] G.A. Olah, Beyond oil and gas: the methanol economy, *Angew. Chem. Int. Ed.* 44 (2005) 2636–2639, <https://doi.org/10.1002/anie.200462121>.
- [6] L. Song, H. Wang, S. Wang, Z. Qu, Dual-site activation of H_2 over $\text{Cu}/\text{ZnAl}_2\text{O}_4$ boosting CO_2 hydrogenation to methanol, *Appl. Catal. B-Environ.* 322 (2023), 122137, <https://doi.org/10.1016/j.apcatb.2022.122137>.
- [7] F. Zhao, L. Fan, K. Xu, D. Hua, G. Zhan, S.-F. Zhou, Hierarchical sheet-like $\text{Cu}/\text{Zn}/\text{Al}$ nanocatalysts derived from LDH/MOF composites for CO_2 hydrogenation to methanol, *J. CO_2 Util.* 33 (2019) 222–232, <https://doi.org/10.1016/j.jcou.2019.05.021>.
- [8] K. Larmier, W.C. Liao, S. Tada, E. Lam, R. Verel, A. Bansode, A. Urakawa, A. Comas-Vives, C. Coperet, CO_2 -to-methanol hydrogenation on zirconia-supported copper nanoparticles: Reaction intermediates and the role of the metal-support interface, *Angew. Chem. Int. Ed.* 56 (2017) 2318–2323, <https://doi.org/10.1002/anie.201610166>.
- [9] Y. Wang, S. Kattel, W. Gao, K. Li, P. Liu, J.G. Chen, H. Wang, Exploring the ternary interactions in $\text{Cu}-\text{ZnO}-\text{ZrO}_2$ catalysts for efficient CO_2 hydrogenation to methanol, *Nat. Commun.* 10 (2019) 1166, <https://doi.org/10.1038/s41467-019-09072-6>.
- [10] Z. Shi, Q. Tan, D. Wu, Enhanced CO_2 hydrogenation to methanol over TiO_2 nanotubes-supported $\text{CuO}-\text{ZnO}-\text{CeO}_2$ catalyst, *Appl. Catal. A-Gen.* 581 (2019) 58–66, <https://doi.org/10.1016/j.apcata.2019.05.019>.
- [11] X.X. Hou, C.H. Xu, Y.L. Liu, J.L. Jun, X.D. Hu, J. Liu, J.Y. Liu, Q. Xu, Improved methanol synthesis from CO_2 hydrogenation over CuZnAlZr catalysts with precursor pre-activation by formaldehyde, *J. Catal.* 379 (2019) 147–153, <https://doi.org/10.1016/j.jcat.2019.09.025>.
- [12] M.M.J. Li, C. Chen, T. Ayvali, H. Suo, J. Zheng, I.F. Teixeira, L. Ye, H. Zou, D. O'Hare, S.C.E. Tsang, CO_2 hydrogenation to methanol over catalysts derived from single cationic layer CuZnGa LDH precursors, *ACS Catal.* 8 (2018) 4390–4401, <https://doi.org/10.1021/acscatal.8b00474>.
- [13] H. Li, L. Wang, Y. Dai, Z. Pu, Z. Lao, Y. Chen, M. Wang, X. Zheng, J. Zhu, W. Zhang, R. Si, C. Ma, J. Zeng, Synergetic interaction between neighbouring platinum monomers in CO_2 hydrogenation, *Nat. Nanotechnol.* 13 (2018) 411–417, <https://doi.org/10.1038/s41565-018-0089-z>.
- [14] F. Jiang, S. Wang, B. Liu, J. Liu, L. Wang, Y. Xiao, Y. Xu, X. Liu, Insights into the influence of CeO_2 crystal facet on CO_2 hydrogenation to methanol over Pd/CeO_2 catalysts, *ACS Catal.* (2020) 11493–11509, <https://doi.org/10.1021/acscatal.0c03324>.
- [15] A. Tsoukalou, P.M. Abdala, D. Stoian, X. Huang, M.G. Willinger, A. Fedorov, C. R. Muller, Structural evolution and dynamics of an In_2O_3 catalyst for CO_2 hydrogenation to methanol: an operando XAS-XRD and in situ TEM Study, *J. Am. Chem. Soc.* 141 (2019) 13497–13505, <https://doi.org/10.1021/jacs.9b04873>.
- [16] S. Wang, P. Wang, Z. Qin, W. Yan, M. Dong, J. Li, J. Wang, W. Fan, Enhancement of light olefin production in CO_2 hydrogenation over In_2O_3 -based oxide and SAPO-34 composite, *J. Catal.* 391 (2020) 459–470, <https://doi.org/10.1016/j.jcat.2020.09.010>.
- [17] H. Zhang, D. Mao, J. Zhang, D. Wu, Regulating the crystal structure of layered double hydroxide-derived Co-In catalysts for highly selective CO_2 hydrogenation to methanol, *Chem. Eng. J.* 452 (2023), 139144, <https://doi.org/10.1016/j.cej.2022.139144>.

- [18] F. Studt, I. Sharafutdinov, F. Abild-Pedersen, C.F. Elkjaer, J.S. Hummelshøj, S. Dahl, I. Chorkendorff, J.K. Nørskov, Discovery of a Ni-Ga catalyst for carbon dioxide reduction to methanol, *Nat. Chem.* 6 (2014) 320–324, <https://doi.org/10.1038/nchem.1873>.
- [19] I. Sharafutdinov, C.F. Elkjaer, H.W. Pereira de Carvalho, D. Gardini, G.L. Chiarello, C.D. Damsgaard, J.B. Wagner, J.-D. Grunwaldt, S. Dahl, I. Chorkendorff, Intermetallic compounds of Ni and Ga as catalysts for the synthesis of methanol, *J. Catal.* 320 (2014) 77–88, <https://doi.org/10.1016/j.jcat.2014.09.025>.
- [20] Y. Men, X. Fang, Q. Gu, R. Singh, F. Wu, D. Danaci, Q. Zhao, P. Xiao, P.A. Webley, Synthesis of Ni_5Ga_3 catalyst by hydrotalcite-like compound (HTlc) precursors for CO_2 hydrogenation to methanol, *Appl. Catal. B-Environ.* 275 (2020), 119067, <https://doi.org/10.1016/j.apcatb.2020.119067>.
- [21] C. Yang, S. Liu, Y. Wang, J. Song, G. Wang, S. Wang, Z.J. Zhao, R. Mu, J. Gong, The interplay between structure and product selectivity of CO_2 hydrogenation, *Angew. Chem. Int. Ed.* 58 (2019) 11242–11247, <https://doi.org/10.1002/anie.201904649>.
- [22] N.H.M.D. Dostagir, R. Rattanawan, M. Gao, J. Ota, J.Y. Hasegawa, A. Fukouka, A. Shrotri, K. Asakura, Co single atoms in ZrO_2 with inherent oxygen vacancies for selective hydrogenation of CO_2 to CO, *ACS Catal.* 11 (2021) 9450–9461, <https://doi.org/10.1021/acscatal.1c02041>.
- [23] Z. Liu, X. Gao, B. Liu, W. Song, Q. Ma, T.-s. Zhao, X. Wang, J.W. Bae, X. Zhang, J. Zhang, Highly stable and selective layered Co-Al-O catalysts for low-temperature CO_2 methanation, *Appl. Catal. B-Environ.* 310 (2022), 121303, <https://doi.org/10.1016/j.apcatb.2022.121303>.
- [24] A.M. Bahmanpour, F. Héroguel, M. Kılıç, C.J. Baranowski, P. Schouwink, L. Röthlisberger, J.S. Luterbacher, O. Kröcher, Essential role of oxygen vacancies of Cu-Al and Co-Al spinel oxides in their catalytic activity for the reverse water gas shift reaction, *Appl. Catal. B-Environ.* 266 (2020), 118669, <https://doi.org/10.1016/j.apcatb.2020.118669>.
- [25] C.S. Li, G. Melaet, W.T. Ralston, K. An, C. Brooks, Y. Ye, Y.S. Liu, J. Zhu, J. Guo, S. Alayoglu, G.A. Somorjai, High-performance hybrid oxide catalyst of manganese and cobalt for low-pressure methanol synthesis, *Nat. Commun.* 6 (2015) 6538, <https://doi.org/10.1038/ncomms7538>.
- [26] L. Wang, E. Guan, Y. Wang, L. Wang, Z. Gong, Y. Cui, X. Meng, B.C. Gates, F. S. Xiao, Silica accelerates the selective hydrogenation of CO_2 to methanol on cobalt catalysts, *Nat. Commun.* 11 (2020) 1033, <https://doi.org/10.1038/s41467-020-14817-9>.
- [27] L. Wang, W. Zhang, X. Zheng, Y. Chen, W. Wu, J. Qiu, X. Zhao, X. Zhao, Y. Dai, J. Zeng, Incorporating nitrogen atoms into cobalt nanosheets as a strategy to boost catalytic activity toward CO_2 hydrogenation, *Nat. Energy* 2 (2017) 869–876, <https://doi.org/10.1038/s41560-017-0015-x>.
- [28] C. Rudolf, B. Dragoi, A. Ungureanu, A. Chiriac, S. Royer, A. Nastro, E. Dumitriu, NAl and CoAl materials derived from takovite-like LDHs and related structures as efficient chemoselective hydrogenation catalysts, *Catal. Sci. Technol.* 4 (2014) 179–189, <https://doi.org/10.1039/c3cy00611e>.
- [29] J. Guo, Z. Wang, J. Li, Z. Wang, In–Ni intermetallic compounds derived from layered double hydroxides as efficient catalysts toward the reverse water gas shift reaction, *ACS Catal.* 12 (2022) 4026–4036, <https://doi.org/10.1021/acscatal.2c00671>.
- [30] G. Yuan, J. Bai, L. Zhang, X. Chen, L. Ren, The effect of P vacancies on the activity of cobalt phosphide nanorods as oxygen evolution electrocatalyst in alkali, *Appl. Catal. B-Environ.* 284 (2021), 119693, <https://doi.org/10.1016/j.apcatb.2020.119693>.
- [31] S. Liu, Y. Yin, Y. Shen, K.S. Hui, Y.T. Chun, J.M. Kim, K.N. Hui, L. Zhang, S.C. Jun, Phosphorus regulated cobalt oxide@nitrogen-doped carbon nanowires for flexible quasi-solid-state supercapacitors, *Small* 16 (2020), e1906458, <https://doi.org/10.1002/smll.201906458>.
- [32] W. Liu, H. Gao, Z. Zhang, Y. Zheng, Y. Wu, X. Fu, J. Su, Y. Gao, CoP/Cu₃P heterostructured nanoplates for high-rate supercapacitor electrodes, *Chem. Eng. J.* 437 (2022), 135352, <https://doi.org/10.1016/j.cej.2022.135352>.
- [33] H. Song, M. Wu, Z. Tang, J.S. Tse, B. Yang, S. Lu, Single atom ruthenium-doped CoP/CDs nanosheets via splicing of carbon-dots for robust hydrogen production, *Angew. Chem. Int. Ed.* 60 (2021) 7234–7244, <https://doi.org/10.1002/anie.202017102>.
- [34] S. Xiao, Y. Zhang, P. Gao, L. Zhong, X. Li, Z. Zhang, H. Wang, W. Wei, Y. Sun, Highly efficient Cu-based catalysts via hydrotalcite-like precursors for CO_2 hydrogenation to methanol, *Catal. Today* 281 (2017) 327–336, <https://doi.org/10.1016/j.cattod.2016.02.004>.
- [35] X. Wang, Y. Liu, T. Zhang, Y. Luo, Z. Lan, K. Zhang, J. Zuo, L. Jiang, R. Wang, Geometrical-site-dependent catalytic activity of ordered mesoporous Co-based spinel for benzene oxidation: In situ DRIFTS study coupled with raman and XAFS spectroscopy, *ACS Catal.* 7 (2017) 1626–1636, <https://doi.org/10.1021/acscatal.6b03547>.
- [36] J. Yang, H.W. Liu, W.N. Martens, R.L. Frost, Synthesis and characterization of cobalt hydroxide, cobalt oxyhydroxide, and cobalt oxide nanodiscs, *J. Phys. Chem. C* 114 (2010) 111–119, <https://doi.org/10.1021/jp908548f>.
- [37] M. Lan, R.M. Guo, Y.B. Dou, J. Zhou, A. Zhou, J.R. Li, Fabrication of porous Pt-doping heterojunctions by using bimetallic MOF template for photocatalytic hydrogen generation, *Nano Energy* 33 (2017) 238–246, <https://doi.org/10.1016/j.nanoen.2017.01.046>.
- [38] C. Wang, C. Zhang, W. Hua, Y. Guo, G. Lu, S. Gil, A. Giroir-Fendler, Catalytic oxidation of vinyl chloride emissions over Co-Ce composite oxide catalysts, *Chem. Eng. J.* 315 (2017) 392–402, <https://doi.org/10.1016/j.cej.2017.01.007>.
- [39] X. Xu, T. Wang, W. Lu, L. Dong, H. Zhang, X. Miao, $\text{Co}_x\text{P}/\text{Co}_3\text{O}_4$ nanocomposite on cobalt foam as efficient bifunctional electrocatalysts for hydrazine-assisted hydrogen production, *ACS Sustain. Chem. Eng.* 9 (2021) 4688–4701, <https://doi.org/10.1021/acssuschemeng.1c00705>.
- [40] Z. Shi, Q. Tan, D. Wu, Mixed-phase indium oxide as a highly active and stable catalyst for the hydrogenation of CO_2 to CH_3OH , *Ind. Eng. Chem. Res.* 60 (2021) 3532–3542, <https://doi.org/10.1021/acs.iecr.0c04688>.
- [41] S. Mo, S. Li, J. Li, Y. Deng, S. Peng, J. Chen, Y. Chen, Rich surface Co(III) ions-enhanced Co nanocatalyst benzene/toluene oxidation performance derived from $\text{Co}^{\text{II}}\text{Co}^{\text{III}}$ layered double hydroxide, *Nanoscale* 8 (2016) 15763–15773, <https://doi.org/10.1039/c6nr04902h>.
- [42] X.G. Song, Y.J. Ding, W.M. Chen, W.D. Dong, Y.P. Pei, J. Zang, L. Yan, Y. Lu, Synthesis and characterization of silica-supported cobalt phosphide catalysts for CO hydrogenation, *Energ. Fuel* 26 (2012) 6559–6566, <https://doi.org/10.1021/ef301391f>.
- [43] M. Tan, X. Wang, X. Wang, X. Zou, W. Ding, X. Lu, Influence of calcination temperature on textural and structural properties, reducibility, and catalytic behavior of mesoporous γ -alumina-supported Ni–Mg oxides by one-pot template-free route, *J. Catal.* 329 (2015) 151–166, <https://doi.org/10.1016/j.jcat.2015.05.011>.
- [44] X. Jia, X. Zhang, N. Rui, X. Hu, C.-j. Liu, Structural effect of Ni/ZrO₂ catalyst on CO_2 methanation with enhanced activity, *Appl. Catal. B-Environ.* 244 (2019) 159–169, <https://doi.org/10.1016/j.apcatb.2018.11.024>.
- [45] Q. Pan, J. Peng, T. Sun, S. Wang, S. Wang, Insight into the reaction route of CO_2 methanation: promotion effect of medium basic sites, *Catal. Commun.* 45 (2014) 74–78, <https://doi.org/10.1016/j.catcom.2013.03.034>.
- [46] L. Deng, Z. Wang, X. Jiang, J. Xu, Z. Zhou, X. Li, Z. You, M. Ding, T. Shishido, X. Liu, M. Xu, Catalytic aqueous CO_2 reduction to formaldehyde at Ru surface on hydroxyl-groups-rich LDH under mild conditions, *Appl. Catal. B-Environ.* 322 (2023), 122124, <https://doi.org/10.1016/j.apcatb.2022.122124>.
- [47] C.Y. Wu, L.L. Lin, J.J. Liu, J.P. Zhang, F. Zhang, T. Zhou, N. Rui, S.Y. Yao, Y. C. Deng, F. Yang, W.Q. Xu, J. Luo, Y. Zhao, B.H. Yan, X.D. Wen, J.A. Rodriguez, D. Ma, Inverse ZrO_2/Cu as a highly efficient methanol synthesis catalyst from CO_2 hydrogenation, *Nat. Commun.* 11 (2020) 5767, <https://doi.org/10.1038/s41467-020-19634-8>.
- [48] J.J. Wang, G.N. Li, Z.L. Li, C.Z. Tang, Z.C. Feng, H.Y. An, H.L. Liu, T.F. Liu, C. Li, A highly selective and stable ZnO-ZrO_2 solid solution catalyst for CO_2 hydrogenation to methanol, *Sci. Adv.* 3 (2017), e1701290, <https://doi.org/10.1126/sciadv.1701290>.
- [49] X. Jia, Y. Zhao, G. Chen, L. Shang, R. Shi, X. Kang, G.I.N. Waterhouse, L.-Z. Wu, C.-H. Tung, T. Zhang, Ni_3FeN nanoparticles derived from ultrathin NiFe-layered double hydroxide nanosheets: an efficient overall water splitting electrocatalyst, *Adv. Energy Mater.* 6 (2016) 1502585, <https://doi.org/10.1002/aenm.201502585>.
- [50] Y. Nakaya, E. Hayashida, H. Asakura, S. Takakusagi, S. Yasumura, K.I. Shimizu, S. Furukawa, High-entropy intermetallics serve ultrastable single-atom Pt for propane dehydrogenation, *J. Am. Chem. Soc.* 144 (2022) 15944–15953, <https://doi.org/10.1021/jacs.2c01200>.
- [51] Y.N. Guo, X. Lu, H.P. Zhang, J. Weng, F. Watari, Y. Leng, DFT study of the adsorption of aspartic acid on pure, N-doped, and Ca-doped rutile (110) surfaces, *J. Phys. Chem. C* 115 (2011) 18572–18581, <https://doi.org/10.1021/jp200598t>.
- [52] C.Y. Shen, K.H. Sun, R. Zou, Q.L. Wu, D.H. Mei, C.J. Liu, CO_2 hydrogenation to methanol on indium oxide-supported rhenium catalysts: The effects of size, *ACS Catal.* 12 (2022) 12658–12669, <https://doi.org/10.1021/acscatal.2c03709>.